Journal of Materials Chemistry B

Accepted Manuscript

ROYAL SOCIETY OF CHEMISTRY

www.rsc.org/materialsB

Journal of Materials Chemistry B RSCPublishing

ARTICLE

Tailored biological retention and efficient clearance of pegylated ultra-small MnO nanoparticles as positive MRI contrast agents for molecular imaging

Cite this: DOI: 10.1039/x0xx00000x

Received 00th January 2012,
Accepted 00th January 2012

DOI: 10.1039/x0xx00000x

www.rsc.org/

P. Chevallier[a], A. Walter[b], A. Garofalo[b], I. Veksler[a], J. Lagueux[c], S. Bégin-Colin[b], D. Felder-Flesch[b], M.-A. Fortin[a]*

A majority of MRI procedures requiring intravascular injections of contrast agents are performed with paramagnetic chelates. Such products induce vascular signal enhancement and they are rapidly excreted by the kidneys. Unfortunately, each chelate is made of only one paramagnetic ion, which, taken individually, has a limited impact on the MRI signal. In fact, the detection of molecular events in the nanomolar range using T_1-weighted MRI sequences requires the design of ultra-small particles containing hundreds of paramagnetic ions per contrast agent unit. Ultra-small nanoparticles of manganese oxide (MnO, 6 – 8 nm diam.) have been developed and proposed as an efficient and at least 1000x more sensitive "positive" MRI contrast agent. However no evidence was found until now, that an adequate surface treatment of these particles could maintain their strong blood signal enhancement, while allowing their rapid and efficient excretion by the kidneys or by the hepatobiliairy pathway. Indeed, the sequestration of MnO particles by the reticuloendothelial system, followed by strong uptake in the liver and in the spleen could potentially lead to Mn^{2+}-induced toxicity effects. For ultra-small MnO particles to be applied in the clinics, it is necessary to develop coatings that also enable their efficient excretion within hours. This study demonstrates for the first time the possibility to use MnO particles as T_1 vascular contrast agents, while enabling the excretion of >70% of all the Mn injected dose after 48h. For this, small, biocompatible and highly hydrophilic pegylated bis-phosphonate dendrons (PDn) were grafted on MnO particles to confer colloidal stability, relaxometric performance, and fast excretion capacity. The chemical and colloidal stability of MnO@PDn particles were confirmed by XPS, FTIR and DLS. The relaxometric performance of MnO@PDns as "positive" MRI contrast agents was assessed (r_1 = 4.4mM^{-1}s^{-1}, r_2/r_1 = 8.6; 1.41 T and 37°C). Mice were injected at 1.21 µg Mn/kg (22 µmol Mn/kg), and scanned in MRI up to 48 h. The concentration of Mn in key organs was precisely measured by neutron activation analysis and confirmed, with MRI, the possibility to avoid RES nanoparticle sequestration through the use of phosphonate dendrons. Due to the fast kidney and hepatobiliairy clearance of MnO particles conferred by PDns, MnO nanoparticles can now be considered for promising applications in T_1-weighted MRI applications requiring less toxic although highly sensitive "positive" molecular contrast agents.

1 Introduction

Magnetic resonance imaging (MRI), one of the most widely available medical imaging modalities, allows high-resolution, whole-body anatomical studies without the use of ionizing radiation. MRI is particularly useful in modern medicine, to differentiate diseased tissues from their surroundings. For this, it is often necessary to inject contrast agents (CAs) which have the capacity to influence the signal from ^{1}H protons. Hydrogen protons contained in water molecules either complexed with, or located in the close vicinity of paramagnetic and superparamagnetic CAs, relax faster. To induce such effects, metallic elements such as iron, manganese and gadolinium are the more commonly used, either in the form of molecules or nanoparticles.

There is a need in molecular medicine, to develop imaging probes that could detect subtle molecular targets at an early stage of different diseases.[1] However, molecular imaging with MRI is still lagging behind in terms of detection sensitivity, compared with nuclear imaging methods such as positron emission tomography (PET). In addition to molecular imaging, new biomedical procedures also require cells to be labeled before their injection *in vivo*, followed by their detection at time points.[2] By bringing hundreds of paramagnetic ions into single CA units, it is possible to considerably enhance the capacity of MRI to detect single molecular targets, or small clusters of locally injected cells.

The development of molecular and cellular medicine has led to the recent development of a new generation of "positive" MRI CAs based on ultra-small Gd, Dy or Mn-containing nanoparticles of diameters in the range 2 - 10 nm.[1, 3-13] By opposition to iron oxide

nanoparticles, ultra-small nanoparticles made of MnO, Gd_2O_3, $GdPO_4$ and $NaGdF_4$ preferentially decrease the longitudinal relaxation time of hydrogen in water molecules, inducing thereby a strong MR signal enhancement in T_1-weighted MRI. With very high fractions of surface atoms, ultra-small particles of gadolinium oxide (Gd_2O_3), gadolinium fluoride (GdF_3, $NaGdF_4$) and manganese oxide (MnO) have emerged as particularly promising candidates for "positively contrasted" molecular and cellular MRI applications.[4-10, 12, 14-17] In fact, small nanoparticles showing high atomic surface ratios induce stronger positive contrast enhancement in MRI.[18] These particles, stable in saline suspensions, are coated with biocompatible and hydrophilic molecules (e.g. PEG, D-glucoronic, dextran). In the recent years, concerns related to the occurrence of nephrogenic systemic fibrosis (NSF), a pathology now associated with the use of gadolinium in MRI, has led to FDA restrictions on the clinical use of this lanthanide element.[19-23] Promising alternatives based on Mn-containing nanoparticles have been developed, to attenuate their toxicological risks.[24-27]

Thermal decomposition has been one of the most widely used and reliable routes to produce relatively large nanoparticle synthesis batches of small and narrow particle size distributions.[8, 11, 28] More recently, one-pot synthesis techniques have also been developed in high boiling point solvents, enabling the production of 1 - 3 nm diam. particles.[4] After synthesis, the particles are covered by ligands or polymers, and suspended in water to measure their hydrodynamic size and properties as MRI contrast agents. For this, both the transverse and the longitudinal relaxation rates ($1/T_2$, $1/T_1$) are measured, and plotted against Mn concentration values to calculate r_2 and r_1 (the "relaxivities"). High r_1 values, and r_2/r_1 values as close as possible to 1 are necessary to demonstrate the potential of "positive" contrast agents for molecular MRI. The first of such studies with MnO particles, was performed by Na et al. [8] PEG-lipid-coated MnO nanoparticles (7 – 25 nm core diameter) were developed, and these studies revealed the strong dependence of the nanoparticle core surface on the longitudinal relaxivity. Unfortunately, very low longitudinal relaxivities were found (r_1 = 0.37 $mM^{-1}s^{-1}$ and r_2/r_1 = 4.7 for 7 nm-diameter MnO nanocrystals at 3 T). The rather low relaxivities nonetheless were used to label and to track rat glioma cells *in vivo*, using T_1-weighted imaging sequences.[29] Then, hollow MnO particles with a ~25 nm-thick porous silica shell were designed as high-stability cell tracking imaging probes.[30] Compared with the latter, the longitudinal relaxivity of these particles appeared slightly increased (r_1= 0.99 $mM^{-1}s^{-1}$ at 11.7 T), allowing the tracking of mesenchymal stem cells over a period of at least 14 days. However, the longitudinal relaxivity of these suspensions was still four (4) to ten (10) times lower than that observed for common clinical CAs such as Gd-DTPA and Gd-DOTA.[31, 32] In fact, coating MnO particles with a layer of silica, considerably affect optimal water exchange between the matrix and the surface paramagnetic ions, which is a key mechanism guaranteeing the performance of "positive" MRI contrast agents.[33] Although Mn^{2+} ions are paramagnetic, MnO nanoparticles in the range 5 – 10 nm, express an antiferromagnetic behaviour.[34]

The most significant increase in relaxivity was reported for MnO particles synthesized with polyol techniques, (r_1 = 7.75 at 1.5T, for PEG-coated MnO particles).[4] However, the relaxometric ratio of these particles were close to that of Mn ions (r_2/r_1 ~10), revealing the possible degradation of MnO cores upon complexation with carboxylic ligands. Indeed, aqueous Mn^{2+} solutions show relaxivities in the order of r_1 = 5.2 $mM^{-1}s^{-1}$ and r_2 = 61 $mM^{-1}s^{-1}$ at 1.41 Tesla and 25°C.[35] Hence, different coating strategies were recently adopted to provide enhanced colloidal stability, with possible improvement on the chemical stability of nanoparticles. [10, 18]

Unfortunately, no clear demonstration of enhanced chemical stability was performed after the coating of MnO particles with carboxymethyldextan and polyethylene sulfonate molecules. An optimal polymeric ligand that could prevent nanoparticle core degradation, while preserving relaxometric properties and colloidal stability is still to be developed. Although manganese is considered less toxic than gadolinium, amounts of Mn^{2+} ions are associated with the occurrence of manganism, a disease that takes symptoms close to that of Parkinson.[36] In order for MnO nanoparticles to be considered as molecular and cellular CAs, the new coating must also prevent the leaching of Mn^{2+}, and favor a strong and rapid excretion of the particles through the urinary and gastrointestinal tracts. Indeed, the transit of MnO particles *in vivo* must be limited to a few hours to minimize the potential toxicity risk to organs. Until now, no comprehensive study has been done to measure the biodistribution of MnO particles.

One class of polymeric ligands could answer the stringent needs for high colloidal stability, optimal relaxometric capacities, and prevention of MnO core degradation: phosphonate dendrons. Indeed, dendron molecules made of short oligoethylene glycol chains have been recently developed, containing phosphonate groups that readily react with metal oxide surfaces.[37-40] In particular, such molecules were successfully used to cover iron oxide nanoparticles. Upon reaction with the phosphonate moieties, the particles present a thin layer of iron phosphonate at their surface. In fact, surface phosphatisation/phosphonatisation has been widely used in a variety of industrial processes, to prevent the chemical degradation of oxidised metal surfaces. In this case, a similar strategy is applied at the nanoscale level to form a chemical phase that is more stable than the parent metal oxide. Moreover, the phosphonate dendron molecules also have a very singular capacity for being recognized and efficiently excreted by the renal and hepatobiliairy systems, as demonstrated in recent MRI studies performed after intravenous injections in the mouse model.[37-40] The procedures evidenced a rapid and strong excretion of particles through the gastro-intestinal tract and through the kidneys.

Not only the PEG chains confer a strong colloidal stability to the particles, it is also expected to generate a very stable phosphonatised coating at the surface of the transition metal oxide cores preventing magnetite Fe_3O_4 from oxidation and preserving the nanoparticles magnetic properties. Manganese phosphonate is chemically much more stable than manganese oxide and the stability of the metal complexes increases with increasing number of phosphonic acid groups.[41] Therefore, coating ultra-small MnO particles with phosphonate dendrons represent a promising way to enhance their chemical and colloidal stability, to enhance their excretion efficiency, and to decrease their potential toxicity.

In this study, a new poly(ethylene glycol)-bis-phosphonate dendron (PDn) of defined structure and composition, was efficiently grafted at the surface of MnO particles. Such dendron bears a phosphonate tweezer to ensure a stronger anchoring at the nanoparticle surface. The efficiency of ligand exchange on MnO particles as well as the strong involvement of phosphonate groups in the chelating process was confirmed by XPS and FTIR. The colloidal stability of the particles was investigated by DLS, and their relaxometric properties, quantified by ^{1}H-NMR. Intravascular (i.v.) injections of MnO@PDn were performed under MRI using the mouse model. Finally, a biodistribution study was performed to quantify the diffusion, excretion and retention of Mn in organs after 24 and 48 h.

2 Experimental

2.1 MnO nanoparticle synthesis

MnO nanoparticles were synthesized by thermal decomposition.[8, 11] Typically, 2.0 g of $Mn(NO_3)_2$*xH_2O (99.99%) and 6.8 g of sodium oleate were dissolved in a mixture of 160 mL ethanol, nanopure water and n-hexane (1:1:2 v/v), refluxed at 70°C for 29h. Thus-formed Mn-oleate complex was decanted, washed with nanopure water twice and dried under vacuum for at least 24h. This complex was then dissolved in 40 mL of hexadecene and sonicated for 2h at 40°C. The mixture was heated under argon flux (5°C /min) until 282°C (kept for 3 min only). The nanoparticles suspension was cooled rapidly to 10°C and then sonicated, then washed using a repeated sequence of ethanol and acetone rinsing intercalated by centrifugation steps (1600g, 10°C, 20 min). Finally, 10 mL of cyclohexane was added which provided a clear suspension of MnO@oleate nanoparticles.

2.2 Dendron synthesis and characterization

A comprehensive description of the PEG-phosphonate dendron synthesis procedure is available in the supporting information.

2.3 Dendron grafting on MnO nanoparticles

The ligand exchange was performed by phase transfer process. For this, 10 mg of MnO@oleate nanoparticles were dispersed in hexane (1mg/mL), and added to an aqueous suspension of phosphonate dendrons (PDn, 10 mg in 10 mL ultrapure water adjusted to pH 3.5 with HCl). The two immiscible phases were magnetically stirred for one night to allow the grafting of PDns at the MnO surface occurring at the water-hexane interface. Ultrafiltration was used to separate MnO@PDn from ungrafted dendrons and from residual oleic acid. For this, regenerated cellulose membranes were used (nominal molecular weight limit: 30kDa; Millipore). After 3 purification steps, the MnO@PDn suspension was collected and lyophilized overnight then preserved in a dry state until colloidal, relaxometric and MRI studies.

2.4 Preparation of MnO@PDn nanoparticle suspensions for DLS, relaxometric and MRI studies

Lyophilised MnO@PDn nanoparticles (70 mg) were suspended in 7 mL of nanopure water (18 MΩ·cm), vortexed 5 min, followed by a mild sonication step (15 min). Then, the particles were further dispersed using a sonication rod (60 MHz, 10 min). Aggregates were eliminated by centrifugation (1000g, 10 min). The resulting suspension was subsequently filtered at 0.45 µm (cellulose acetate syringe filter, VWR Int. North America), then at 0.2 µm (polyethersulfone, VWR Int., North America). The hydrodynamic diameter of the particles was measured by DLS. The final nanoparticle suspension was adjusted to 154 mM NaCl (1 M NaCl). The amount of Mn in the 154 mM NaCl solution was measured by graphite furnace atomic absorption spectroscopy (GF-AAS; Perkin-Elmer Analyst 800). Prior to these measurements, the samples were digested in nitric acid (trace metal, Fisher) and hydrogen peroxide (H_2O_2, Sigma-Aldrich).

2.5 Particle size analysis

The MnO nanocore size distributions were assessed by transmission electron microscopy (TEM, 120 or 200 keV: JEOL-1230 and JEOL JEM-2100F, before and after dendronisation. In brief, the suspensions were diluted in methanol (1:10). Three (3) µL were deposited on carbon-coated copper grids (Canemco-Marivac, Lakefield, Canada) then dried before imaging. The ImageJ software particle size analysis tool was used to measure the distribution of the oxide cores. The hydrodynamic diameter of MnO@PDn in water and in 154 mM NaCl were confirmed by dynamic light scattering (DLS, Malvern Zetasizer 173°, t = 25°C). The viscosity and refractive index of water was set to 0.8872 cp and the MnO refractive index of the particles was fixed to 2.160 (used to transform intensity in volume and number). The hydrodynamic diameter was calculated from the average of six measurements.

2.6 Physico-chemical characterisation: FTIR and XPS

Aqueous and methanol suspensions of MnO@PDn were deposited on a Si crystal then dried and analyzed by ATR-FTIR (Agilent Cary 660 FTIR, Agilent Technologies, USA), equipped with a deuterated L-alanine doped triglycine sulfate (DLa-TGS) detector and a Ge coated KBr beam splitter. The particles as well as the dendron were also characterized by XPS (PHI 5600-ci spectrometer, Physical Electronics U.S.A., MN, U.S.A.). Samples of MnO@PDn particles were deposited and dried on silicon substrates previously cleaned by TL2 and TL1 solutions (TL2 solution, a mixture of ultrapure water, 30% hydrogen peroxide (H_2O_2, Fluka, ON, Canada) and concentrated hydrochloric acid Fisher, Canada) (6:1:1), at 80°C for 10 min and TL1 solution, a mixture of ultrapure water, 30% H_2O_2 and 25% ammonia (Fisher, IL, USA) (5:1:1), at 80°C for 10 min). The wafers were thoroughly rinsed with ultrapure water and anhydrous ethanol, quickly dried under medical air. MnO@PDn particles deposited on these substrates were then analyzed by X-ray photoelectron spectroscopy (XPS) using a monochromatic aluminum X-ray source for survey spectra (0−1400 eV) at 200 W, while high resolution spectra of C1s, O1s, N1s and P2p were obtained by using a standard magnesium X-ray source (1253.6 eV), at 150 W. For neither analysis was applied charge neutralization. The detection was performed at 45° with respect to the surface normal and the analyzed area was 0.005 cm^2. The spectrometer work function was adjusted to give 285.0 eV for the main C (1s) peak. Curve fittings for both the survey and the high resolution C (1s) peaks were determined by means of least squares minimization procedure employing Gaussian-Lorentzian functions and a Shirley-type background.

2.7 ^{1}H relaxometric measurements

The stock solution of MnO@PDn particles in 154 mM of NaCl were diluted (to 5, 10, 15 and 25% v/v) and distributed in NMR tubes. Then, longitudinal and transverse relaxation times (T_1 and T_2) were measured at 60 MHz (1.41 T) using a Bruker MiniSpec relaxometer. The temperature was set to 37°C for all measurements. Finally, the relaxation rates ($1/T_1$ and $1/T_2$) were plotted against Mn concentration values (from GF-AAS), and relaxivities (r_1 and r_2) were calculated from the slope of the graphs.

2.8 Colloidal stability assay

MnO@PDn suspensions in water and in 154 mM NaCl, were left at room temperature and measured over time with DLS (24h, 48h, 7, 14, 21 days).

2.9 In vitro contrast media MRI studies

The stock solution of MnO@PDn particles in 154 mM of NaCl were diluted (to 5, 10, 15 and 25% v/v) and distributed in 500 µl-tubes immersed in water. The tubes were inserted in a 60-mm RF coil and imaged at 25°C with a 1 T small-animal MRI system (M2M, Aspect Imaging, Netanya, Israel). T_1-weighted 2D spin-echo sequences were used, as follows: TE = 10.8ms; TR = 400ms, 700ms and 1000ms; f_α=90°; FOV= 70 mm; 1.9 mm slices with 0.1 mm gap; dwell time =16 µs, matrix: 200 X 200; 3 exc. A series of T_2-weighted 2D spin echo sequence was also performed (TE = 50, 75 ms and 100 ms; TR = 2500 ms; f_α=90°; 1 exc.), that confirmed the weak performance of MnO particles as "negative" contrast agents.

2.10 In vivo MRI and biodistribution studies

Aliquots of the MnO@PDn suspensions in 154 mM NaCl were adjusted to a concentration of 4.4 ± 0.1 mM Mn. All animal experiments were conducted under the guidelines of Université Laval and CHUQ's animal ethical committee. Four week-old balb/c female mice (Charles River, Montreal, Canada) were anaesthetised with isoflurane and placed on a dedicated bed inside a 3.5 cm-diameter RF coil while their respiration was monitored. Animals were cannulated in the caudal tail vein (30G, winged needle), and connected to a catheter prewashed with heparin and connected to the contrast media syringe (280µm ID Intramedic™ Polyethylene Tubing PE-10, 60 cm, total volume: 60 µL). Prior to injections, the animals were scanned twice using a T_1-weighted 2D spin echo sequence, with the following parameters: TE = 18.3ms; TR = 800ms; f_α=90°; FOV= 90 mm; 0.7 mm slices with 0.1 mm gap; dwell time =25 µs, matrix: 400 X 320; duration: 4min16s. At time t = 0, the animals (3) were injected with 100 µL of nanoparticle suspension (4.4 ± 0.1 mM Mn; total Mn injected = 0.44 µmol, or 24.1 µg). The same MR sequence was repeated for at least 120 minutes. These animals were scanned again at t = 8, 24, 48 hours (static scans, 4.16 min each). A total of three (3) animals were injected for each nanoparticle product. For signal analysis, raw signal data were extracted, and regions of interest (ROIs), drawn over sections of the abdominal aorta, left kidney, bladder and gall bladder. The mean signal intensity was calculated using Image J software (version 1.44m; Wayne Rasband, National Institutes of Health, USA). Signal enhancement ratios were calculated as follows:

$$\text{Ratio}_{t=x} = \frac{\text{Signal}_{t=x}}{\text{Signal}_{t=0}} \qquad \text{Equation 1}$$

Finally, after 48 hours the mice were euthanatized by intracardiac exsanguination. A selection of organs were collected and weighted, prior to Mn quantification by neutron activation analysis (Slowpoke Laboratory, École Polytechnique de Montréal). To complete the 48h biodistribution data with an intermediate point, a group of mice (3) were injected and euthanatized at t = 24, and measured for Mn organ levels.

3 Results and discussion

3.1. Synthesis and particle size studies

Ultra-small MnO particles, synthesized by thermal decomposition, are initially covered with oleate, a hydrophobic molecule. Then, oleate is removed upon reaction with PDns through a ligand exchange and phase transfer process. In the present study, highly water soluble and biocompatible bifunctional dendrons were used. A comprehensive schematic representation of the dendron synthesis is summarised in Schemes S1 and S2 (in the supporting information), as well as a detailed description of synthesis and characterisation at each step (Figures S1 – S4). The phosphonate dendron **13** obtained as a result of this synthesis chain is represented in Figure 1.a and Scheme S2. Compared to other dendrons previously reported in the literature, **13** features a bisphosphonic acid tweezer. This coupling agent was designed to allow a stronger and more efficient binding to NPs, compared to monophosphonate dendrons,[37, 42, 43] and thus better long-term colloidal stability in physiological media.[44-46] The dendron also features a hydrophilic PEGylated structure with carboxylic acid as terminal groups for nanoparticle functionalization. The bisphosphonate precursor **8** (Figure 1) was obtained starting from commercially available ethyl 3,5-dimethylbenzoate (see supporting information), and the coupling of the PEGylated dendron **4** (see ESI) with bisphosphonate **8** was obtained via a classical peptide-type coupling (Figure1 and ESI). The PEGylated dendron **12** was finally fully deprotected in one step in the presence of trimethylsilyl bromide to give COOH-functionalized bisphosphonic acid **13**.

The size of MnO cores was measured with TEM before (8.4 ± 0.8 nm) and after ligand exchange (6.3 ± 0.7 nm) with PDns, as shown in Figure 1 (on at least 100 particles for each sample). The grafting mechanism had a significant impact on the mean diameter of the MnO oxide cores. This represents a mean volume decrease of 57.8%. This diameter is attributed to the presence of a manganese hydroxide layer (~ 1 nm thick) forming at the surface of the particles upon reaction with water, and prior to reaction with PDn. Indeed, Mn hydroxide is more susceptible to degrade under interactions with phosphonate groups, resulting in Mn^{2+} leaching during the ligand exchange process. After PDn reaction, traces of the crystal lattice of MnO cores were still visible at the center of MnO particles (Figure 2a, white arrow, HRTEM 200 keV). The MnO crystal cores were unfortunately too small to allow the extraction of a clear electron diffraction pattern. The apparent thickness of the coating indicated the formation of a thick, P-containing (EDS data, Figure S5) inorganic layer at the interface between the MnO crystal and the PDns chains. At certain places in the TEM grid, a limited presence of a lower density P-containing phase (EDS confirmed) was identified, attributed to the presence of unreacted PDn (Figure 2b, dashed white arrow).

After suspension of the particles in water and in saline, volume-weighted hydrodynamic diameters of 13.4 ± 1.6 nm (34.5 nm in intensity) and 30.7 ± 2.3 (55.0 in intensity) were found, respectively (Figure 2.c,d). For the particles suspended in water, at day 0, the Z-average was 24.8 ± 0.2 and the PDI value was 0.260 ± 0.005. After 21 days, similar values were found (25.4 ± 0.3 and the PDI value was 0.262 ± 0.005). For the particles suspended in saline, at day 0, the Z-average was 41.8 ± 0.5 and the PDI value was 0.235 ± 0.008. After 21 days, similar values were found (41.4 ± 0.5 and the PDI value was 0.286 ± 0.004).

Number-weighted data (Figure 2.e) indicated much lower hydrodynamic diameters, in agreement with the expected values for MnO@PDn (8.1 ± 1.7 nm and 20.4 ± 1.1 nm). Because PDns contain two phosphonate moieties, cross-reactions between two nanoparticles cannot be ruled-out. This possibly explains the limited presence of small aggregates suggested by the larger-than-expected hydrodynamic sizes diameters (volume-weighted data, Figure 2.b and d). Finally, the colloid was very sable in both saline and deionised water for at least 21 days, with larger hydrodynamic sizes in the saline solution (Figure 2.c,d,e). No sign of flocculation was found during the repeated DLS analysis. The zeta potential,

measured in 154 mM NaCl and at pH 6, was – 18.6 mV. This confirms the fact that strong electrostatic forces add up to the steric repulsion induced by the PEG chains, and confer a robust colloidal stability to the suspension.

3.2. Physico-chemical surface analysis of MnO@PDn particles

FTIR analysis was performed to assess the efficiency of ligand exchange (Figure 3). The intensity of the main peaks associated to MnO@oleate particles was strongly modified, in particular the CH vibration bands around 2922 and 2852 cm^{-1} as well as asymmetric (υ_{as} (CO_2^-)) and symmetric (υ_s (CO_2^-)) carboxylate stretching bands at 1553 cm^{-1} and 1429 cm^{-1}. These bands present on the MnO@oleate spectrum were largely attenuated in the MnO@PDn spectrum, confirming the elimination of oleate, and the efficiency of ligand exchange. Upon PDn grafting, new bands appeared, characteristic of the chemical structure of PDn: 3097 cm^{-1} associated to the CH vibration in the aromatic ring; 1740 cm^{-1} associated to the C=O band of the carboxylic acid function; 1648 cm^{-1} associated to the C=O band of the amide link. The peak at 1097 cm^{-1} can be assigned mainly to the C-O vibration in the PEG structure and to a possible contribution from aromatic C-C bonds. This confirms the strong presence of PEG grafted at the MnO particles.

The peaks in the range 1280 - 700 cm^{-1} are mainly associated to phosphonate bands (Figure 3.b). Phosphonate derivatives bands were difficult to precisely associate with given MnO-phosphonate chelation types. Indeed, each band can possibly refer to two or more vibration types. As an example, P=O and P-OH are susceptible to be strongly affected by their chemical environment. Others are affected by the pH (PO_3^{2-}, PO_2^-). Chemical links also affect the bands (either free, H or metallic links), leading to asymmetric and symmetric vibrations for a same group. It was nonetheless possible to ascribe the band at 1234 cm^{-1} to the P=O bond.[38, 40, 47] The strong intensity decrease after complexation with MnO, as well as a splitting of this band at 1221 cm^{-1} suggest either its involvement in the chelation process or hydrogen bonding of P=O with the surface. Because each PDn contains a bisphophonate head, one P=O group can be involved in chelation and/or hydrogen bonding whereas the other one remains free. Therefore, the P=O band was not fully attenuated. Also, as indicated by the TEM results (Figure 2.b), the presence of a certain fraction of unreacted PDn in the samples may contribute to maintain this band.

The bands at 1076 cm^{-1} and 993 cm^{-1} are mainly attributed to PO-O^- and PO-OH,[48] and they changed after complexation with MnO. Indeed, peak shoulders were observed at 1045 cm^{-1} and 938 cm^{-1} respectively. This is in accordance with previous results,[40, 47, 49] and confirms the involvement of the phosphonate group in the chelation. However, the band at 993 cm^{-1} was not fully attenuated after complexation with MnO, suggesting that a certain fraction of unreacted phosphonate groups is still present after reaction with MnO. Because P=O and PO-O^- bands appear changed after chelation, this is a strong evidence that the type of chelation is at least bidendate.[50]

Whereas EDS (described in section 3.1), performed with an electron probe of a few nm^2 only, allowed to confirm the strong presence of P at the outer surface of particles, XPS spectra were used to study the nature of the chemical binding occurring between the phosphonate groups and the MnO surface. XPS has a relatively large X-ray probe (the total area irradiated by the X-rays, ~1 mm^2), therefore MnO-oleate, bisphosphonate dendrons (PDn) and MnO@PDn samples were dispersed on flat substrates, then analysed by XPS to provide elemental information of about 5 – 10 nm in depth. XPS spectra survey results are presented in Table 1 and high resolution spectra of O (1s) and P (2p) in Figure 4. The O/C ratios of MnO-oleate particles (0.301) were higher than the theoretical O/C ratio (0.111) expected for oleate only. Because the analytical penetration depth of XPS is about 5 nm, the higher oxygen content was mainly attributed to MnO. High oxygen contents also reflect the thinness of the oleate coating (see Figure 1.d). After dendron grafting, the relative fraction of Mn strongly decreased, in agreement with the expected thicker dendrons coatings. The difference of thicknesses between dendron and oleate coatings is clearly illustrated in Figure 1.d and Figure 1.e. During the grafting process in water, a network of hydrogen bonds forms between the bisphosphonates and the carboxylates. This arrangement likely generates a bilayer of dendritic molecules. Increasing hydrodynamic diameters observed after 21 days in water, seem to corroborate this hypothesis. In 154 mM NaCl however, the strong concentration of Na^{2+} counter-ions impacts on the hydrogen bonds, as reflected by the decreasing hydrodynamic diameters (Figure 2.c). The presence of a broad band at 3600 - 3200 cm^{-1} in the MnO@PDn FTIR spectrum (Figure 2), absent from the PDn spectrum, also indicates the strong presence of hydrogen bonds.

In XPS O (1s) high resolution spectra, the band at 531.5 eV was attributed to P=O, P-O-Mn, MnOH ; that at 532.9 – 533.2 eV to -C-O- and to oxygen in –COOH, -CONH; the one at 534.0-534.5 eV to P-OH.[51-53] The contribution at 531.5 eV strongly increased after dendron grafting on the MnO nanoparticles, mainly due to the contribution of P-O-Mn, MnOH (Table 1). The contribution at 534.5 eV, associated to P-OH, decreased. This indicates the involvement of the P-O bond in the chelation.[49, 51, 53] The involvement of phosphonate groups in the chelation process was also evidenced by the chemical shift of the P2p band, from 133.9 eV for the free dendron to 133.2 eV (0.7 eV shift) for PDn chelated on MnO nanoparticles (Figures 4.b and 4.d, respectively). This shift is consistent with previous results evidenced with dendronised iron oxide nanoparticles and its value larger than 0.5 confirms the deprotonation of both -P-OH terminations and thus the formation of at least two P−O−Fe bonds.[47] Finally, due to its very low detection sensitivity, the Mn 3s peak could not be efficiently revealed. However, the main Mn2p peak was centred at 641.6 eV for the MnO@dendron, compared to 641.3 eV for MnO@oleate. This indicates that Mn^{2+} is the main oxidation state in both systems.

3.3. Relaxometric analysis and in vitro MRI performance

The relaxometric rates ($1/T_1$, $1/T_2$) of MnO@PDn suspensions were calculated, and the results were plotted against the concentration of manganese (Figure 5). Longitudinal relaxivity values (r_1 = 4.4 $mM^{-1}s^{-1}$) in the same order than for Gd-DTPA and Gd-DOTA were found, much higher than for PEG-lipid-coated MnO particles of 7 nm core diameter reported in the literature (0.37 $mM^{-1}s^{-1}$ at 3T).[8] The dendron coating confers to MnO particles of 7 – 8 nm diam., relaxometric properties relatively similar to that demonstrated by dimercaptosuccinic acid-PEG and carboxymethyldextran coatings, which are efficient "positive" CAs for T_1-weighted MRI. Indeed, MnO particles of similar size (7-8 nm core diam.) coated with DMSA-PEG or carboxymethyldextran, have relaxometric ratios in the same order as MnO@PDns (r_2/r_1 ~ 4; r_1= 3.4 $mM^{-1}s^{-1}$ for DMSA-PEG, and r_2/r_1 = 5.3; r_1 = 5.4 $mM^{-1}s^{-1}$ for carboxymethyldextran, both measured at 1.5 Tesla).[11, 18] As a comparison, the expected relaxivities for Mn^{2+} ions measured at 1.41 Tesla and 25°C are r_1 = 5.2 $mM^{-1}s^{-1}$ and r_2 = 61 $mM^{-1}s^{-1}$.[35] Therefore, the relaxometric ratios measured for MnO@PDn are more favorable to T_1-weighted imaging compared to that of Mn^{2+}

ions only (r_2/r_1~ 10 at 1.41 T). Finally, the MnO@PDn suspensions imaged in MRI provided a clear positive contrast enhancement with an optimum value around 0.66 mM Mn (Figure 3).

3.4. Dynamic contrast-enhanced MRI experiments

Mice were injected with 100 µL of MnO@PDn (4.4 mM Mn, T_1 = 48 ms), which corresponds to a 24.2 µg-dose of Mn per 20 g-animal (0.44 µmol Mn/injection). The amount of injected Mn was kept in the same order as the indicated dosage for Mn-DPDP (Telascan), 5 – 10 µmolMn/kg.[54] Before administration of the CA, a T_1-weighted 2-D MRI spin echo scan was performed, and coronal images of the animals were acquired. Then, the animals were injected and a pronounced blood signal increase was observed, allowing for an excellent visualization of the abdominal vasculature (Figure 6). The mice were scanned in continuous during 120 minutes, then at time points (t = 8h, 24h, 48h). Up to 48 hours (end of the experiment), the animals did not show any sign of discomfort, and no apparent change was noted in their behaviour and feeding.

Coronal images are represented in Figure 4 for slices corresponding to the gall bladder (a), kidneys (b) and urinary bladder (c). In these images, regions of interest (ROIs) were drawn over each of these organs, and the signal was integrated over each area. The results were plotted in the form of signal-enhancement graphs (Figure 7). Ultra-small MnO@PDn particles provided a clear and persistent vascular signal enhancement effect in the first 20 minutes following their injection, with a maximum at ~ 10 minutes (Figure 7.a). Usually, no significant blood signal enhancement is observed in the first 5 minutes following i.v. injections of $MnCl_2$ (free Mn^{2+} ions).[54] Therefore, the persistence of vascular signal enhancement is clearly due to the presence of PEG-PDn-stabilised nanoparticles. Also, the measurement of nanoparticle vascular concentration is not as straightforward when using iron oxide nanoparticles. The "negative" contrast behaviour of dendron-coated iron oxide nanoparticles does not allow the correlation of signal change with nanoparticle concentration.[38, 40] Therefore, the blood retention of PEG-dendron-coated nanoparticles had never been measured until now. The present study demonstrates that vascular concentrations of PDn-stabilised MnO-particles can be followed with MRI, which is a very strong advantage in the perspective of developing molecular imaging probes based on metal oxide nanoparticles. In fact, this is the first study to provide a comprehensive *in vivo* monitoring and biodistribution profile of PEG-dendron-stabilised nanoparticles.

The signal enhancement profiles of MnO@PDn in the liver suggest a biodistribution profile of Mn that is very different to what is typically observed for i.v. injected Mn^{2+} ions. In rats injected with 100 µmol of $MnCl_2$/kg of body weight, levels of Mn in the liver reached 38% of the total injected dose after 30 minutes. HSA-coated MnO particles of hydrodynamic diameter ~ 39 nm, also showed a rapid and massive liver uptake after one hour only, which was attributed to sequestration by the RES.[55] Such a dramatic influx of Mn in the liver was not observed in the present study (Figure S6). Then, after one (1) hour, a strong signal enhancement was observed in the gall bladder (full arrowhead, Figure 6), but not in the liver. This brilliance persisted over at least 8 hours (Figure 6 and 7.c). After 24 hours however, the Mn concentration in the gall bladder seemed attenuated. In the blood, Mn^{2+}, whether free or bound to proteins, is efficiently cleared by the liver and any excess is normally excreted in the bile.[36] MnO@PDn apparently follows the same elimination pathway, however not following the same kinetics.

The excretion of Mn^{2+} also occurs through the gastrointestinal mucosa and pancreatic secretions. Virtually none is excreted through the kidneys.[56-58] Evidences were found of strong urine elimination from the first minutes following MnO@PDn administration (Figure 6). Urinary excretion is usually not observed after i.v. administration of $MnCl_2$.[54] However, evidences of urinary excretion were recently reported for PDn-grafted iron oxide nanoparticles injected in mice.[38, 40] In the present study, because MnO@PDN particles are a "positive" contrast agent, the kinetics of nanoparticle kidney and urine transit were measured with MRI. Signal enhancement in the urine reached a peak value of 1.78 after 60 minutes (Figure 7.b). In the kidneys, signal enhancement was present in both the cortex and in the pyelon. This was confirmed by the comparison of signal enhancement profiles obtained for the kidneys (Figure 5.c) and for the urinary bladder (Figure 7.d). Therefore, it can be concluded that grafting PDns at the surface of ultra-small particles is a promising strategy to enhance the excretion of molecular imaging probes, which is particularly critical when potentially toxic ions (such as Mn^{2+}) could be involved. Finally, no evidence was found of contrast enhancement in the brain (data not shown).

3.5. Manganese biodistribution study

After DCE-MRI studies, the levels of manganese in organs were measured at t = 24h and t = 48h, using neutron activation analysis. In fact, this is the first study that provides a comprehensive biodistribution study of ultra-small MnO nanoparticles. Until now, there had been no organ biodistribution performed with i.v.-injected MnO nanoparticles, and few data has been reported on the transit of these particles through the urinary, gastro-intestinal or hepatobiliairy pathways.

The total amount of Mn injected in animals corresponds to 1.21 mg Mn/kg of body weight (22 µmol Mn/kg). As shown in Table 2, very low manganese levels were found in the blood after 24 hours, which is consistent with the DCE-MRI results. The highest concentrations of Mn were found in the feces, intestine, gall bladder, kidneys and stomach, in decreasing order of contents. In spite of the high endogenous presence of Mn expected in the liver and in the spleen, limited concentrations of Mn were found in these organs, as well as in the lungs. In fact, the tissues rich in mitochondria – such as liver, kidney, heart, and pancreas, contain the highest levels of endogenous manganese.[59, 60] The low Mn contents in the liver confirm that RES sequestration is not the preponderant nanoparticle elimination pathway of MnO@PDn.

Recently, Huang, Chen et al investigated with MRI and PET, the tumour contrast enhancement potential of albumin-coated MnO particles (r_1 = 1.97 $mM^{-1}s^{-1}$; d_H = 39.2 ± 3.6 nm). Massive uptake by the liver was evidenced in the PET data, as soon as one hour after injection.[55] These results indicated that MnO particles, as many other inorganic core nanoparticles in that size range, are strongly sequestrated by the RES if they are not adequately coated with molecules preventing or delaying their opsonisation. RES-sequestrated nanoparticles are more susceptible to remain in the organism for longer periods, which in the case of Mn^{2+}-containing nanoparticles, would represent a toxicological risk.

On the contrary, MnO@PDn nanoparticles are not significatively uptaken in the liver. Therefore, grafting PDns at the surface of nanoparticles enhance their biocompatibility profile, and makes them applicable to biomedical procedures. Based on Mn concentration measurements in organs, we calculated the rate of Mn decrease between 24h and 48h. The strongest Mn elimination values were found for the following organs: bladder, heart, liver, kidneys, gall

bladder and lungs. At 48h, very strong concentrations of Mn were found in the feces, intestine, as well as in the stomach (possible contamination at the extraction, during separation from the gastrointestinal tract). All results converge to hepatobiliairy elimination as the main pathway for the clearance of MnO@PDns.

Then, we calculated the retention of MnO@PDn in the heart, lungs, liver, gall bladder, kidneys, spleen and in the bladder, and expressed it units of % of injected dose (% I.D., Table 3). For this, the endogenous amounts of Mn in mice organs, well documented in the literature (summarised in the supporting info, Table S1), were subtracted from the neutron activation analysis data obtained for each organ. The endogenous Mn concentrations reported in the literature are as follows: of 0.18 – 0.4 µg Mn/g for the heart, 0.18 µg Mn/g for the lungs, 1- 2.1 µg Mn/g for the liver, 0.94 – 1.6 µg Mn/g for the kidneys, and 0.4 – 0.45 µg Mn/g for the spleen.[61-63] The levels of Mn in the intestine, feces, and stomach are highly dependent on the diet of animals and therefore these values are variable. As an indication, Damadian et al found Mn levels of 4.27 µg Mn/g for the stomach, and 3.36 µg Mn/g for the gastro-intestinal tracts.[61] Because of the usually high and variable endogenous Mn contents in stomach and in the gastro-intestinal tract, we did not include these organs in the final calculation of MnO@PDn organ retention.

After 24 hours, the strongest fractions of MnO@PDn were found in the gallbladder (25.7%), in the kidneys (21%), in the liver (14.8%), and in the heart (7.9%). After 48 hours, these data had decreased to 11%, 8.3%, 5.7%, and 3.0%, respectively. By comparison, rats injected with 100 µmol of $MnCl_2$/kg of body weight showed a total Mn retention of 50% after 7 days. In the present study, for the interval included between 24h and 48h, and considering only the group of seven (7) organs mentioned in Table 3, the total % I.D. decrease was 42.7%. Indeed, the body clearance of MnO@PDns particles through the hepatobiliairy pathway occurs much faster than for $MnCl_2$, with a % of total I.D. retention estimated to 31% after 48h. The very low amount of Mn found in the spleen, further confirms that PDn-pegylated MnO nanoparticles are not taken up by the RES, and could therefore be considered as advantageous probes for molecular MR imaging.

4 Conclusions

Ultra-small MnO particles were pegylated with small, biocompatible and highly hydrophilic bis-phosphonate dendrons (PDns). The new MnO colloids are very stable, and they induce "positive" MRI contrast enhancement potentially advantageous in molecular imaging procedures. In this study, we demonstrated that PDn-grafted ultra-small MnO nanoparticles are eliminated through the hepatobiliairy pathway, and this considerably mitigates the risk that represents the potential sequestration of MnO particles by the reticuliendothelial system. Evidences of urinary excretion were also found. Applications of MnO nanoparticles as imaging probes in medicine have always appeared hindered by their potential toxicity. The present study confirms that MnO nanoparticles adequately coated with stabilizing molecules favouring their efficient and rapid elimination through faeces and urine, could find promising uses as "positive" MRI CAs. Finally, PDn grafting could advantageously be applied to other metal oxide nanoparticles of potential interest in medicine, and in particular on the development of multi-modality tracers for molecular imaging (e.g. with radioactive, fluorescent and bioactive functionalities).

Acknowledgements

M.A.F. is grateful for NSERC, FRQS and Centre Québécois des Matériaux Fonctionnels (CQMF) for their financial support to this work. This work was financially supported by the CNRS, the University of Strasbourg and the French Ministry of research (MENRT fellowship to A. Walter). We also thank the European Union (European Regional Development Fund – ERDF) in the framework of the INTERREG.IV Upper Rhine Program (Nanomatrix project, fellowship to A. Garofalo). Dr Claire Billotey (U.Claude Bernard, Lyon), is gratefully acknowledged for fruitful discussions. The authors would like to thank the valuable contributions of Jean-Philippe Masse (TEM), Dr Cornelia Chilian (neutron activation analysis) and Mélissa Guignard (MRI animal care technician, CHUQ) to this work.

Notes and references

[a] Axe médecine régénératrice, Centre de recherche du Centre hospitalier universitaire de Québec (CR-CHUQ),10 rue de l'Espinay, Québec, G1L 3L5, Canada, Département de génie des mines, de la métallurgie et des matériaux and Centre de recherche sur les matériaux avancés (CERMA), Université Laval, Québec, G1V 0A6, Canada.
[b] Institut de Physique et Chimie des Matériaux de Strasbourg (IPCMS), UMR 7504 CNRS- Université de Strasbourg, 23, rue du Loess, BP 43, 67034 Strasbourg Cedex 2, France.
[c] Axe médecine régénératrice, Centre de recherche du Centre hospitalier universitaire de Québec (CR-CHUQ), 10 rue de l'Espinay, Québec, G1L 3L5, Canada.
*Corresponding author: marc-andre.fortin@gmn.ulaval.ca, Fax: (+1) 418-656-5343; Tel: (+1) 418-656-8682

†Electronic Supplementary Information (ESI) available: dendron synthesis, and characterisation: ^{1}H, ^{13}C, ^{31}P NMR and MALDI data for compounds 1 – 13, mass spectrum of dendron, EDS spectrum of MnO@PDns , MRI signal (SI) follow-up studies after injection of MnO@PDn, in the liver and data from the literature on manganese levels in untreated mice. See DOI: 10.1039/b000000x/

1. C. Q. Tu and A. Y. Louie, *Wires Nanomed Nanobi*, 2012, **4**, 448-457.
2. W. J. Rogers, C. H. Meyer and C. M. Kramer, *Nat Clin Pract Cardiovasc Med*, 2006, **3**, 554-562.
3. F. Q. Hu and Y. S. Zhao, *Nanoscale*, 2012, **4**, 6235-6243.
4. J. Y. Park, E. S. Choi, M. J. Baek, G. H. Lee, S. Woo and Y. Chang, *Eur J Inorg Chem*, 2009, 2477-2481.
5. J. L. Bridot, A. C. Faure, S. Laurent, C. Riviere, C. Billotey, B. Hiba, M. Janier, V. Josserand, J. L. Coll, L. V. Elst, R. Muller, S. Roux, P. Perriat and O. Tillement, *J Am Chem Soc*, 2007, **129**, 5076-5084.
6. M. Ahren, L. Selegard, A. Klasson, F. Soderlind, N. Abrikossova, C. Skoglund, T. Bengtsson, M. Engström, P. O. Käll and K. Uvdal, *Langmuir*, 2010, **26**, 5753-5762.
7. H. B. Na and T. Hyeon, *J Mater Chem*, 2009, **19**, 6267-6273.
8. H. B. Na, J. Lee, H., K. An, Y. I. Park, M. Park, I. S. Lee, D. H. Nam, S. T. Kim, S. H. Kim, S. W. Kim, K. H. Lim, K. S. Kim, S. O. Kim and T. Hyeon, *Angewandte Chemie Int. Ed.*, 2007, **46**, 5397-5401.
9. T. D. Schladt, K. Schneider, M. I. Shukoor, F. Natalio, H. Bauer, M. N. Tahir, S. Weber, L. M. Schreiber, H. C. Schroder, W. E. G. Muller and W. Tremel, *J Mater Chem*, 2010, **20**, 8297-8304.
10. C. C. Huang, N. H. Khu and C. S. Yeh, *Biomaterials*, 2010, **31**, 4073-4078.
11. M. Letourneau, M. Tremblay, L. Faucher, D. Rojas, P. Chevallier, Y. Gossuin, J. Lagueux and M. A. Fortin, *J Phys Chem B*, 2012, **116**, 13228-13238.
12. L. Faucher, M. Tremblay, J. Lagueux, Y. Gossuin and M. A. Fortin, *ACS applied materials & interfaces*, 2012, **4**, 4506-4515.
13. Y. Gossuin, A. Hocq, Q. L. Vuong, S. Disch, R. P. Hermann and P. Gillis, *Nanotechnology*, 2008, **19**, 475102.

14. M. Letourneau, M. Tremblay, L. Faucher, D. Rojas, P. Chevallier, Y. Gossuin, J. Lagueux and M. A. Fortin, *J Phys Chem B*, 2012, **116**, 13228-13238.
15. M. J. Baek, J. Y. Park, W. Xu, K. Kattel, H. G. Kim, E. J. Lee, A. K. Patel, J. J. Lee, Y. Chang, T. J. Kim, J. E. Bae, K. S. Chae and G. H. Lee, *ACS applied materials & interfaces*, **2**, 2949-2955.
16. L. Faucher, Y. Gossuin, A. Hocq and M. A. Fortin, *Nanotechnology*, 2011, **22**, 295103.
17. D. Kryza, J. Taleb, M. Janier, L. Marmuse, I. Miladi, P. Bonazza, C. Louis, P. Perriat, S. Roux, O. Tillement and C. Billotey, *Bioconjugate Chem*, 2011, **22**, 1145-1152.
18. J. Park, D. Bang, E. Kim, J. Yang, E. K. Lim, J. Choi, B. Kang, J. S. Suh, H. S. Park, Y. M. Huh and S. Haam, *Eur J Inorg Chem*, 2012, 5960-5965.
19. A. K. Abu-Alfa, *Advances in chronic kidney disease*, 2011, **18**, 188-198.
20. C. Kennedy, C. Magee, E. Eltayeb, C. Gulmann and P. J. Conlon, *Irish medical journal*, 2010, **103**, 208-210.
21. A. Y. Chen, M. J. Zirwas and M. P. Heffernan, *Journal of drugs in dermatology : JDD*, 2010, **9**, 829-834.
22. K. H. Kim, J. R. Fonda, E. V. Lawler, D. Gagnon and J. S. Kaufman, *American journal of kidney diseases : the official journal of the National Kidney Foundation*, 2010, **56**, 458-467.
23. D. R. Martin, S. K. Krishnamoorthy, B. Kalb, K. N. Salman, P. Sharma, J. D. Carew, P. A. Martin, A. B. Chapman, G. L. Ray, C. P. Larsen and T. C. Pearson, *Journal of magnetic resonance imaging : JMRI*, 2010, **31**, 440-446.
24. D. P. J. Pan, A. H. Schmieder, S. A. Wickline and G. M. Lanza, *Tetrahedron*, 2011, **67**, 8431-8444.
25. M. Kueny-Stotz, A. Garofalo and D. Felder-Flesch, *Eur J Inorg Chem*, 2012, 1987-2005.
26. D. Pan, S. D. Caruthers, A. Senpan, A. H. Schmieder, S. A. Wickline and G. M. Lanza, *Wiley interdisciplinary reviews. Nanomedicine and nanobiotechnology*, 2010.
27. A. P. Koretsky and A. C. Silva, *NMR in biomedicine*, 2004, **17**, 527-531.
28. J. Park, K. J. An, Y. S. Hwang, J. G. Park, H. J. Noh, J. Y. Kim, J. H. Park, N. M. Hwang and T. Hyeon, *Nature Materials*, 2004, **3**, 891-895.
29. A. A. Gilad, P. Walczak, M. T. McMahon, H. B. Na, J. H. Lee, K. An, T. Hyeon, P. C. van Zijl and J. W. Bulte, *Magnetic resonance in medicine : official journal of the Society of Magnetic Resonance in Medicine / Society of Magnetic Resonance in Medicine*, 2008, **60**, 1-7.
30. T. Kim, E. Momin, J. Choi, K. Yuan, H. Zaidi, J. Kim, M. Park, N. Lee, M. T. McMahon, A. Quinones-Hinojosa, J. W. M. Bulte, T. Hyeon and A. A. Gilad, *J Am Chem Soc*, 2011, **133**, 2955-2961.
31. P. Caravan, *Chemical Society Reviews*, 2006, **35**, 512-523.
32. P. Caravan, J. J. Ellison, T. J. McMurry and R. B. Lauffer, *Chem Rev*, 1999, **99**, 2293-2352.
33. T. D. Schladt, K. Koll, S. Prufer, H. Bauer, F. Natalio, O. Dumele, R. Raidoo, S. Weber, U. Wolfrum, L. M. Schreiber, M. P. Radsak, H. Schild and W. Tremel, *J Mater Chem*, 2012, **22**, 9253-9262.
34. M. A. Morales, R. Skomski, S. Fritz, G. Shelburne, J. E. Shield, M. Yin, S. O'Brien and D. L. Leslie-Pelecky, *Phys Rev B*, 2007, **75**.
35. J. Vymazal, J. W. M. Bulte, J. A. Frank, G. Dichiro and R. A. Brooks, *Jmri-Journal of Magnetic Resonance Imaging*, 1993, **3**, 637-640.
36. J. Crossgrove and W. Zheng, *NMR in biomedicine*, 2004, **17**, 544-553.
37. B. Basly, D. Felder-Flesch, P. Perriat, C. Billotey, J. Taleb, G. Pourroy and S. Begin-Colin, *Chemical communications (Cambridge, England)*, 2010, **46**, 985-987.
38. G. Lamanna, M. Kueny-Stotz, H. Mamlouk-Chaouachi, C. Ghobril, B. Basly, A. Bertin, I. Miladi, C. Billotey, G. Pourroy, S. Begin-Colin and D. Felder-Flesch, *Biomaterials*, 2011, **32**, 8562-8573.
39. B. Basly, D. Felder-Flesch, P. Perriat, G. Pourroy and S. Begin-Colin, *Contrast media & molecular imaging*, 2011, **6**, 132-138.
40. B. Basly, G. Popa, S. Fleutot, B. P. Pichon, A. Garofalo, C. Ghobril, C. Billotey, A. Berniard, P. Bonazza, H. Martinez, D. Felder-Flesch and S. Begin-Colin, *Dalton Transactions*, 2013, **42**, 2146-2157.
41. B. Nowack, *Water research*, 2003, **37**, 2533-2546.
42. C. Queffelec, M. Petit, P. Janvier, D. A. Knight and B. Bujoli, *Chemical Reviews*, 2012, **112**, 3777-3807.
43. C. Ghobril, G. Popa, A. Parat, C. Billotey, J. Taleb, P. Bonazza, S. Begin-Colin and D. Felder-Flesch, *Chem Commun (Camb)*, 2013, **49**, 9158-9160.
44. Y. Lalatonne, C. Paris, J. M. Serfaty, P. Weinmann, M. Lecouvey and L. Motte, *Chem Commun (Camb)*, 2008, 2553-2555.
45. R. Torres Martin de Rosales, R. Tavare, A. Glaria, G. Varma, A. Protti and P. J. Blower, *Bioconjug Chem*, 2011, **22**, 455-465.
46. L. Sandiford, A. Phinikaridou, A. Protti, L. K. Meszaros, X. Cui, Y. Yan, G. Frodsham, P. A. Williamson, N. Gaddum, R. M. Botnar, P. J. Blower, M. A. Green and R. T. de Rosales, *Acs Nano*, 2013, **7**, 500-512.
47. E. Smecca, A. Motta, M. E. Fragala, Y. Aleeva and G. G. Condorelli, *J Phys Chem C*, 2013, **117**, 5364-5372.
48. H. Benbenishty-Shamir, R. Gilert, I. Gotman, E. Y. Gutmanas and C. N. Sukenik, *Langmuir*, 2011, **27**, 12082-12089.
49. L. C. Thomas and Chittend.Ra, *Spectrochim Acta a-M*, 1970, **A 26**, 781-&.
50. P. H. Mutin, G. Guerrero and A. Vioux, *Cr Chim*, 2003, **6**, 1153-1164.
51. G. Beamson and D. Briggs, ed. Wiley, Chichester, 1992.
52. A. A. Guay-Begin, P. Chevallier, L. Faucher, S. Turgeon and M. A. Fortin, *Langmuir : the ACS journal of surfaces and colloids*, 2011.
53. M. Textor, L. Ruiz, R. Hofer, A. Rossi, K. Feldman, G. Hahner and N. D. Spencer, *Langmuir*, 2000, **16**, 3257-3271.
54. G. Elizondo, C. J. Fretz, D. D. Stark, S. M. Rocklage, S. C. Quay, D. Worah, Y. M. Tsang, M. C. Chen and J. T. Ferrucci, *Radiology*, 1991, **178**, 73-78.
55. J. Huang, J. Xie, K. Chen, L. H. Bu, S. Lee, Z. Cheng, X. G. Li and X. Y. Chen, *Chem Commun*, 2010, **46**, 6684-6686.
56. M. Kato, *Quarterly journal of experimental physiology and cognate medical sciences*, 1963, **48**, 355-369.
57. J. P. Mahoney and W. J. Small, *The Journal of clinical investigation*, 1968, **47**, 643-653.
58. W. T. Burnett, Jr., R. R. Bigelow, A. W. Kimball and C. W. Sheppard, *The American journal of physiology*, 1952, **168**, 620-625.
59. I. H. Tipton and M. J. Cook, *Health physics*, 1963, **9**, 103-145.
60. H. Fore and R. A. Morton, *The Biochemical journal*, 1952, **51**, 600-603.
61. G. N. Ling, T. Kolebic and R. Damadian, *Physiological chemistry and physics and medical NMR*, 1990, **22**, 1-14.
62. Y. Takehara, H. Sakahara, H. Masunaga, S. Isogai, N. Kodaira, M. Sugiyama, H. Takeda, T. Saga, S. Nakajima and I. Sakata, *Magnetic resonance in medicine : official journal of the Society of Magnetic Resonance in Medicine / Society of Magnetic Resonance in Medicine*, 2002, **47**, 549-553.
63. M. A. Dubick and C. L. Keen, *Toxicology letters*, 1983, **17**, 355-360.

Table 1. XPS analyses of Mn, O, N, C and P elements at the surface of MnO@PDn.

Sample	Mn2p	O1s	N1s	C1s	P2p	O/C	P/N
MnO@oleate	4.6	20.4 (5.5% Mn-O) [13.8% C-O] {1.1% COOH}	-	67.7 (63.8% C-C / CH) [1.8% C-O] {2.1% C=O}	-	0.301	-
MnO@PDn	0.9	33.9 (8.1% P=O / Mn-O-P / Mn-OH) [24.6% C-O] {1.2% P-OH}	0.9	60.1 (18.2% C-C / CH) [37.5% C-O] {4.3% C=O}	2.1	0.564	2.333
Dendron (PDn)	-	27.4 (2.3% P=O) [22.1% C-O] {3.0% C=O}	1.1	67.3 (35.6% C-C / CH) [24.8% C-O] {3.3% C=O}	1.3	0.407	1.182

***The balance in XPS for MnO@oleate, MnO@dendron, and dendron were Si, Na and Cl.

Table 2. Manganese levels in organs after 24 and 48h following injections of MnO@PDns (0.44 μmol Mn/animal)

	Organs	24 h μg Mn / g organ	± std. dev	48h μg Mn / g organ	± std. dev	% change
1	blood	0.06	0.04	0.04	0.03	-28
2	heart	2.2	0.1	0.80	0.06	-175
3	lungs	0.84*	0.03*	0.35	0.10	-139
4	liver	3.9	0.3	1.46	0.04	-165
5	gallbladder	6.50*	0.03*	2.8*	1.0*	-130
6	stomach	4	2	13	9	70
7	kidneys	5.3	0.6	2.09	0.05	-156
8	bladder + urine	0.6	0.2	0.11	0.01	-405
9	intestine	32	10	24	4	-31
10	spleen	0.46	0.04	0.34*	0.02*	-37
11	feces	149	56	114	24	-31
12	pancreas	6	2	3.0	0.4	-86

All measurements performed in triplicate except for * (2 measures)

Table 3. Retention of MnO@PDn in organs, in % of injected dose (I.D.) of MnO@PDs (0.44 μmol Mn/animal) at t = 0. Except for gall bladder and bladder, the expected endogenous Mn levels were subtracted from the measured Mn values to calculate % I.D.

Organs	24 h		48 h		% change
	% I.D.	±	% I.D.	±	
heart	7.9%	0.3%	3.0%	0.2%	-62
lungs	2.3%	0.1%	1.1%	0.3%	-50
liver	14.8%	1.3%	5.7%	0.1%	-61
gallbladder	25.7%	0.1%	11%	4%	-56
kidneys	21%	2%	8.3%	0.2%	-60
bladder + urine	1.1%	0.3%	0.14%	0.02%	-88
spleen	0.70%	0.07%	1.06%	0.05%	52

Tailored biological retention and efficient clearance of pegylated ultra-small MnO nanoparticles as positive MRI contrast agents for molecular imaging

P. Chevallier[a], A. Walter[b], A. Garofalo[b], I. Veksler[a], J. Lagueux[c], S. Bégin-Colin[b], D. Felder-Flesch[b], M.-A. Fortin[a]*

[a] Axe médecine régénératrice, Centre de recherche du Centre hospitalier universitaire de Québec (CR-CHUQ),10 rue de l'Espinay, Québec, G1L 3L5, Canada, Département de génie des mines, de la métallurgie et des matériaux and Centre de recherche sur les matériaux avancés (CERMA), Université Laval, Québec, G1V 0A6, Canada.
[b] Institut de Physique et Chimie des Matériaux de Strasbourg (IPCMS), UMR 7504 CNRS- Université de Strasbourg, 23, rue du Loess, BP 43, 67034 Strasbourg Cedex 2, France.
[c] Axe médecine régénératrice, Centre de recherche du Centre hospitalier universitaire de Québec (CR-CHUQ), 10 rue de l'Espinay, Québec, G1L 3L5, Canada.
*Corresponding author: marc-andre.fortin@gmn.ulaval.ca, Fax: (+1) 418-656-5343; Tel: (+1) 418-656-8682

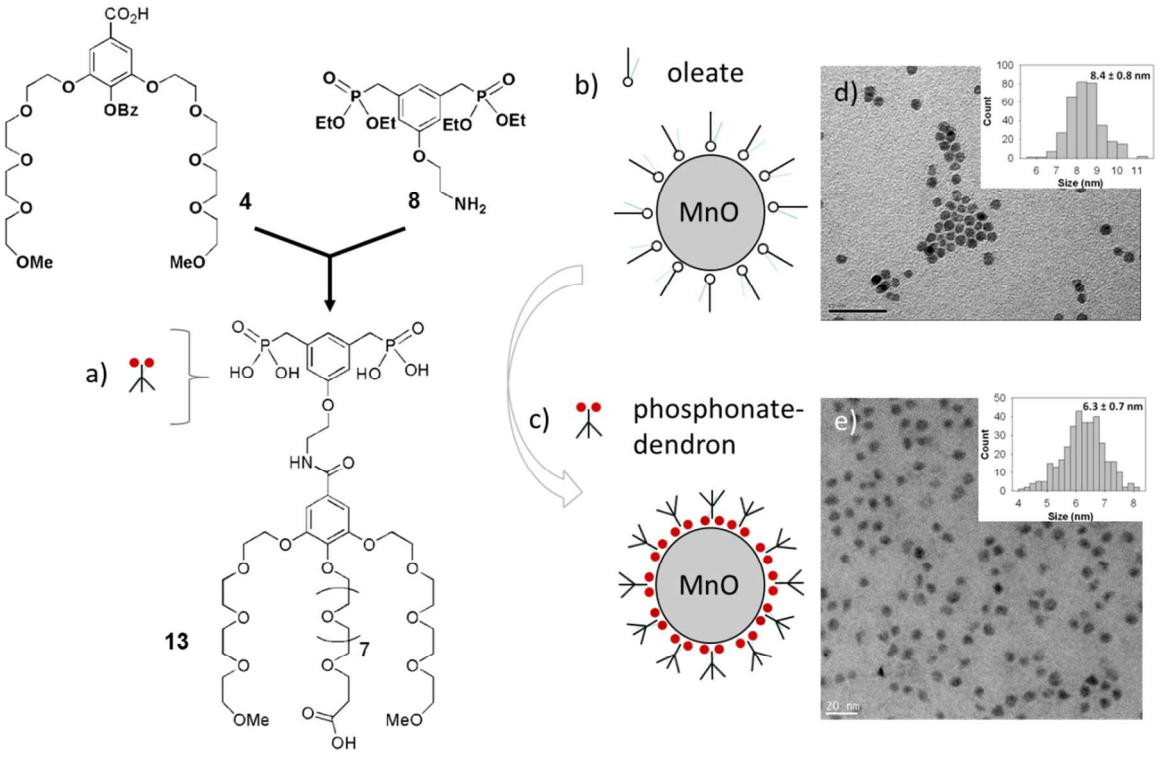

Figure 1. a) Schematic representation of the bisphosphonate dendron synthesis and grafting procedure. Oleate molecules initially coating the MnO nanocrystals (b), are efficiently removed from the surface and replaced by bisphosphonate dendrons (c). TEM images of MnO particles before (d) and after (e) PDn grafting.

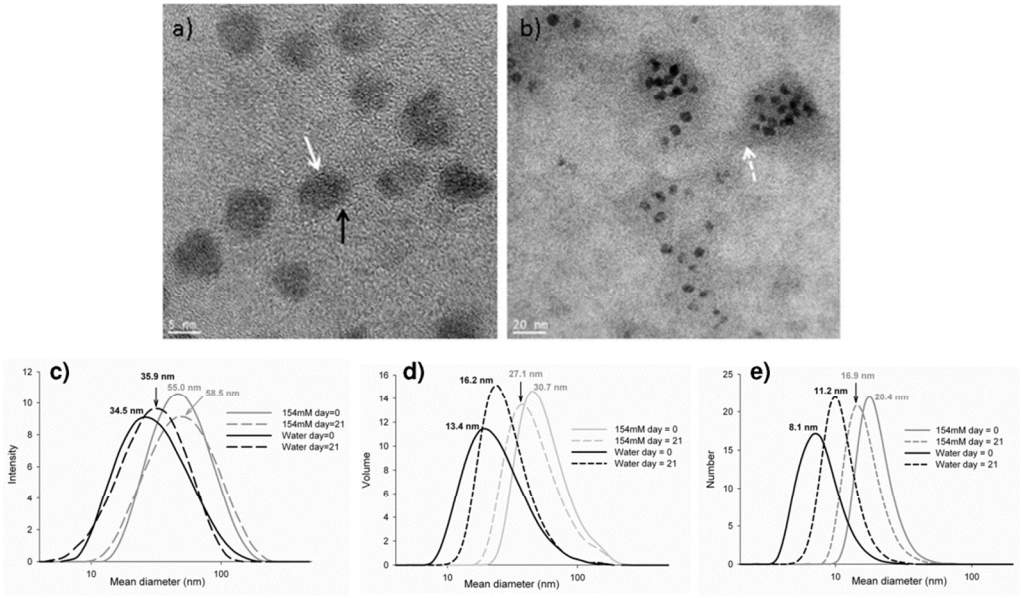

Figure 2. a) HRTEM images of MnO@PDn particles with evidences of crystallographic lattices (white arrow). b) A moderate number of small MnO@PDn agglomerates were found, as well as evidences of the limited presence of unreacted PDn (dashed white arrow). Hydrodynamic diameter measurements in water and in 154 mM NaCl c) in intensity, d) in volume and e) in number

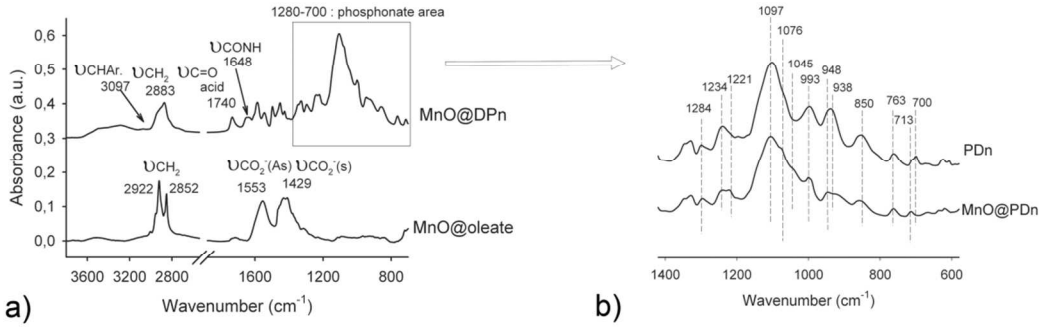

Figure 3. a) FTIR spectra of MnO@oleate and MnO@PDn particles; b) close-up on the phosphonate peaks area for the free dendron and the grafted MnO@PDn particles.

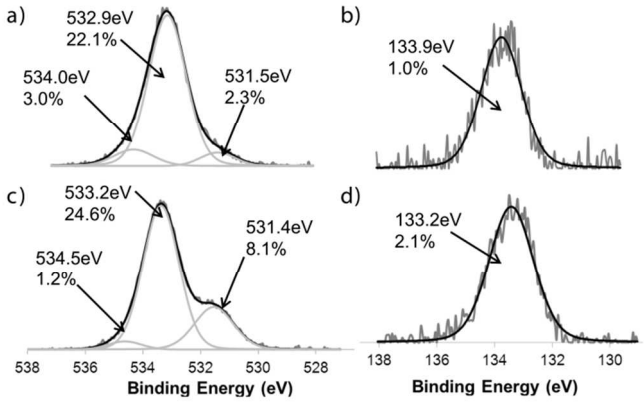

Figure 4. O1s and P2p high resolution spectra of dendron (a, b) and MnO@dendron (c,d)

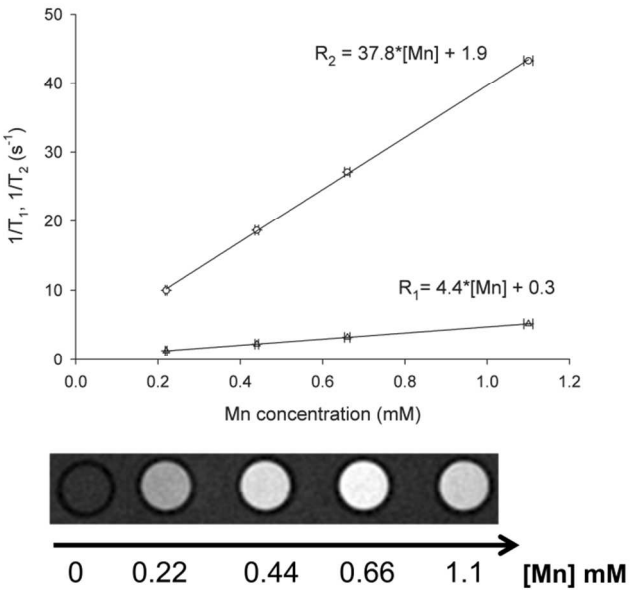

Figure 5. Relaxivity curves (a) and contrast enhancement in T_1-w. MRI (TE/TR: 11/400 ms) for MnO@PDn solutions in 154mM NaCl.

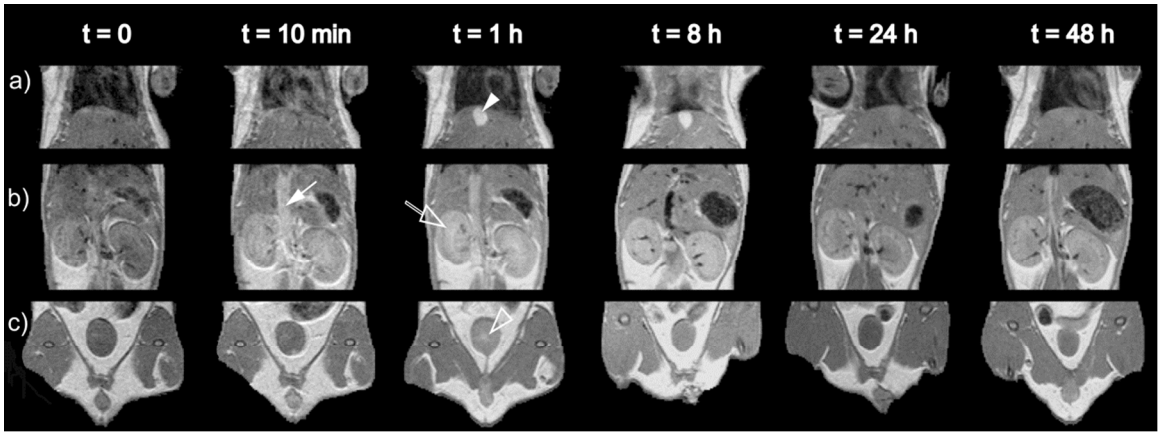

Figure 6. MRI images of MnO@PDn-injected mice at t = 0, 10 min, 1, 8, 24 and 48h, for a) the gall bladder, b) the kidneys, c) the urinary bladder. The full arrowhead points to the gall bladder; the full arrow points to the abdominal aorta; the empty arrow points to the kidneys; the empty arrowhead points to urinary bladder.

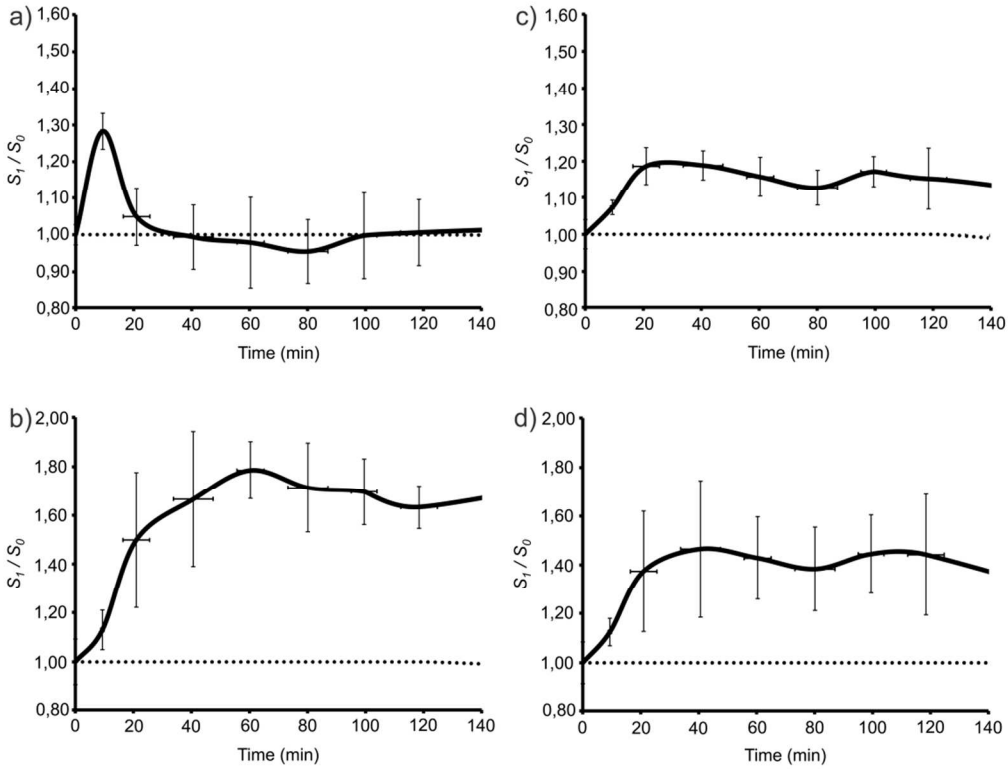

Figure 7. MRI signal (SI) follow-up studies after injection of MnO@PDn, for a) blood (abdominal vessels), b) gall bladder, c) kidneys and d) bladder. Each point represents the average of at least three measurements performed in three mice. The data were pooled in 10-min. time intervals, and horizontal error bars indicate the extremes of each interval.

Tailored biological retention and efficient clearance of pegylated ultra-small MnO nanoparticles as positive MRI contrast agents for molecular imaging

P. Chevallier[a], A. Walter[b], A. Garofalo[b], I. Veksler[a], J. Lagueux[c], S. Bégin-Colin[b], D. Felder-Flesch[b], M.-A. Fortin[a]*

[a] Axe médecine régénératrice, Centre de recherche du Centre hospitalier universitaire de Québec (CR-CHUQ),10 rue de l'Espinay, Québec, G1L 3L5, Canada, Département de génie des mines, de la métallurgie et des matériaux and Centre de recherche sur les matériaux avancés (CERMA), Université Laval, Québec, G1V 0A6, Canada.
[b] Institut de Physique et Chimie des Matériaux de Strasbourg (IPCMS), UMR 7504 CNRS- Université de Strasbourg, 23, rue du Loess, BP 43, 67034 Strasbourg Cedex 2, France.
[c] Axe médecine régénératrice, Centre de recherche du Centre hospitalier universitaire de Québec (CR-CHUQ), 10 rue de l'Espinay, Québec, G1L 3L5, Canada.
*Corresponding author: marc-andre.fortin@gmn.ulaval.ca, Fax: (+1) 418-656-5343; Tel: (+1) 418-656-8682

Table of Contents

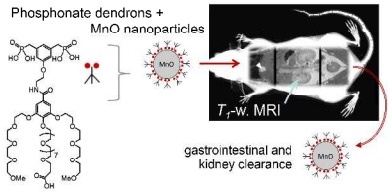

Ultra-small MnO nanoparticles pegylated with bis-phosphonate dendrons are efficient positive contrast agents in T_1-w. MRI. Intravenous injections of MnO@PDn provide prolonged vascular signal enhancement in MRI, followed by efficient excretion through the hepatobiliairy and urinary ways. The potential toxicity of MnO nanoparticles is thereby considerably decreased, and could allow their use as biomedical MR probes.